energies

MDPI

Article

Local Structure Optimization Design of Floating Offshore Wind Turbine Platform Based on Response Surface Analysis

Yajun Ren [1], Mingxuan Huang [2], Jungang Hao [1], Jiazhi Wang [2], Shuai Li [1], Ling Zhu [1], Haisheng Zhao [2,*] and Wei Shi [2]

[1] China Renewable Energy Engineering Institute, Beijing 100120, China; janeryj@outlook.com (Y.R.); zhuling@creei.cn (L.Z.)
[2] State Key Laboratory of Coastal and Offshore Engineering, Dalian University of Technology, Dalian 116024, China; mingxuanh@163.com (M.H.); jzwang@mail.dlut.edu.cn (J.W.); weishi@dlut.edu.cn (W.S.)
* Correspondence: hzhao@dlut.edu.cn

Abstract: The floating platform is a critical component of the floating offshore wind turbine (FOWT), and its internal structure design plays a key role in ensuring the safe operation of the FOWT. In this study, the local model of the floating platform was firstly parameterized, and a response surface model was obtained by conducting an orthogonal test. The response surface model was then optimized using a gradient descent algorithm. Finally, the internal structure arrangement was validated through a safety calibration. The optimization results indicate that the maximum stress of the optimized model is reduced by 22.12% compared to the original model, while maintaining the same mass, centroid, and other mass-related parameters. The optimization significantly improves the safety of the structure and provides valuable references for the design and construction of a FOWT platform.

Keywords: floating offshore wind turbine; structural strength; response surface optimization; gradient descent method

Citation: Ren, Y.; Huang, M.; Hao, J.; Wang, J.; Li, S.; Zhu, L.; Zhao, H.; Shi, W. Local Structure Optimization Design of Floating Offshore Wind Turbine Platform Based on Response Surface Analysis. *Energies* **2024**, *17*, 6316. https://doi.org/10.3390/en17246316

Academic Editor: Francesco Castellani

Received: 5 November 2024
Revised: 8 December 2024
Accepted: 11 December 2024
Published: 14 December 2024

1. Introduction

Developing offshore wind power is a crucial strategy to support the national "double carbon" goals and drive the transition to sustainable energy [1]. As a green, renewable, and sustainable energy source, offshore wind power has garnered increasing attention worldwide. Over the past decade, the global offshore wind power market has experienced an average annual growth rate of 27%, with a cumulative installed capacity reaching 75.2 GW by the end of 2023 [2]. According to statistics, about 80% of the world's wind energy resources are located in sea areas deeper than 50 m, where offshore wind energy offers several advantages over traditional onshore wind power, including higher wind energy density, minimal impact on terrestrial ecosystems, and no land use conflicts. As a result, the development of floating offshore wind turbines (FOWTs) has emerged as an effective approach to develop far-reaching sea wind energy, playing an increasingly important role in ensuring global energy security [3]. This is of great strategic importance for the development of deep offshore resources [4].

The performance of the floating body must meet strict requirements to ensure safe operation in the complex and changeable deep-sea environment. In the research on the normal operation of offshore wind turbines (OWTs), an exploration of the structural design of the floating offshore wind turbine platform helps to improve the safety redundancy of the floating body. As a result, many scholars have recently focused on improving the motion response and safety performance of offshore platforms. Tian et al. [5] investigated the correlation between the main scale of the structure and the objective function, where the structural weight and motion response are regarded as the objective function and the NSGA-II algorithm is used to improve the computational efficiency. Yang et al. [6] studied

the reliability-based optimization of a tripod-supported OWT under dynamic constraints. The meta-model technology was used to replace the finite element calculation method to improve the efficiency of the calculation. Structural mass was used as the objective function, while uncertain factors such as material properties, geometry, and load types were included as random variables. Their approach, combining global optimization with Monte Carlo simulation, demonstrated effective optimization of both structural weight and dynamics.

Saeed et al. [7] proposed a new design scheme for a multi-functional floating platform based on a density-based topology optimization method, which can significantly improve the stiffness and durability of the platform and reduce the total mass of the new optimized structure to 40.82% of the main structure. Chen et al. used a fully coupled aerodynamic–hydrodynamic net mooring time-domain model constructed by combining AQWA and FAST with the open-source code F2A for a preliminary analysis of a turreted deep-sea aquaculture vessel powered by wind energy [8]. Lu et al. [9] used topology optimization to develop a lightweight design for the tripod structure of OWTs. Their method notably reduced weight while improving fatigue resistance compared to the original structure. Karimi et al. [10] applied a multi-objective genetic algorithm (GA) optimization method to evaluate different platforms to find the minimum cost and maximum performance wind turbine form under specified environment conditions and sea state spectrum. Lee et al. [11] developed a neural response surface method (NRSM) for objective optimization problems, which is used to optimize the generated response surface combined with the second-generation non-dominated sorting genetic algorithm (NSGA-II).

Ferri et al. [12] designed a multi-objective optimization program to determine the optimal substructure configuration for a 10 MW FOWT at a specific site. Choi et al. [13] used a design of experiments (DOE) approach to minimize the number of calculation models required, employing a GA with neural network approximation to optimize the platform and substructure of the 3 MW spar wind turbine system, resulting in a reliable structural form. Additionally, Benifla et al. [14] developed an optimization framework for the floating foundation of OWTs based on a genetic algorithm. Dou et al. [15] explored a conceptual optimization design framework for the floating foundation with a mooring system, capable of accurately determining designs that meet optimal conditions. Leimeister et al. [16] developed a method to optimize the floating concept by using the global limit state, where the NSGA-II optimization algorithm is selected to find the optimal design solution. Hall et al. [17] built an optimization framework for the support structure of a FOWT based on a genetic algorithm. Furthermore, Hegseth et al. [18] proposed a linearized aerodynamic-hydrodynamic-servo-elastic FOWT model combined with gradient optimization and analytical derivative methods.

As mentioned above, current studies on optimizing the main dimensions of floating bodies primarily focus on motion performance and total structural mass. The internal stiffeners, bulkheads, and ribs of the platform contribute over 60% of the floating body's total mass, where their size and arrangement play a critical role in ensuring structural safety, while the corresponding local structure optimization design is seldom carried out previously.

In this study, an A-type floating body was selected as the research subject, with the aim of optimizing its structural configuration to reduce maximum structural stress under extreme sea conditions, based on an initially optimized model. First, the relationship between internal structure variables, such as structural mass, centroid position, and maximum stress, are determined through an orthogonal test. Based on the above results, the optimal configuration relationship of reinforcement and other structures of floating foundation structure are determined through the optimization process, employing the gradient descent algorithm. Additionally, the optimized structure must be subjected to a strength verification test to ensure its reliability under extreme sea conditions. Finally, the study outlines a comprehensive optimal design methodology for the floating platform of FOWTs, based on the steps and findings described below.

2. Theoretical Methods

FOWTs are located in a complex and changing marine environment and are constantly subjected to the combined effects of wind and wave loads. These external forces have a significant impact on the stability and performance of the wind turbine. In this study, the theories of wind and wave are introduced as follows.

2.1. Wind Load Calculation Theory

Due to the different heights of each part of the fan, the average wind speed will also be different, generally showing a gradient change rule [19]. The formula is as follows:

$$\overline{v}(z) = \overline{v}(h)\left(\frac{z}{h}\right)^{1/n} \tag{1}$$

where z is the altitude; h is the reference height above sea level; $v(h)$ is the average wind speed at the reference height h; $v(z)$ is the average wind speed at altitude z; and n is the wind profile index of sea surface roughness, whose value is related to the time distance and offshore distance when measuring wind speed is generally between 7~13 m/s.

In the strength analysis, wind load is an important factor to be considered. During the normal operation of the FOWT, the area swept by the wind turbine blades should be included when calculating the wind pressure area [20]. However, under extreme conditions, when the wind turbine is in a downwind shutdown state, the wind load acting on the tower becomes the dominant factor. In such cases, the wind load on the wind turbine tower can be expressed as Equation (2) [21]:

$$F = 0.5 C_S C_H \rho_\alpha A V^2 \tag{2}$$

where C_S is the shape coefficient of the component; C_H is the height coefficient, which can refer to the specification DNVGL-OS-C301 [20]; ρ_α is the air density; A is the frontal projection area of the windward surface of the component; and V is the wind speed.

2.2. Wave Field Calculation Theory

In this study, the wave load is calculated through the three-dimensional potential flow theory [22], which accounts for drag, inertial, and diffraction forces. This theory is particularly suitable for calculating the interaction of large-scale structures and waves when the structure is stationary. The velocity potential function of the wave field is shown in Equation (3) [23]:

$$\Phi^{(1)}(x,y,z) = \Phi_I^{(1)}(x,y,z) + \Phi_D^{(1)}(x,y,z) + \Phi_R^{(1)}(x,y,z) \tag{3}$$

where $\Phi^{(1)}$ denotes the first-order velocity potential; $\Phi_D^{(1)}$ is the first-order diffraction potential; and $\Phi_R^{(1)}$ denotes the first-order radiation potential.

Φ_I is calculated as below:

$$\Phi_I = \frac{igA}{\omega} \cdot \frac{cosh(Kz+d)}{cosh(Kd)} \cdot e^{-K(xcos\beta + ysin\beta)} \tag{4}$$

where g is the acceleration of gravity; A is the amplitude; K is the wave number; d is the water depth; and β is the wave direction angle.

The boundary conditions for solving the velocity potential of diffracted and radiation waves are as follows:

(1) Diffracted wave

Free surface condition:

$$-\omega^2 \Phi^D + g\frac{\partial \Phi^D}{\partial z} = 0 \; z = 0 \tag{5}$$

Object surface condition:

$$\left.\frac{\partial \Phi^D}{\partial n}\right|_S = -\left.\frac{\partial \Phi^I}{\partial n}\right|_S \tag{6}$$

Seabed boundary condition:

$$\left.\frac{\partial \Phi^D}{\partial z}\right|_{z=-h} = 0 \tag{7}$$

Infinite condition:

$$\lim_{R\to\infty} \sqrt{R}\left(\frac{\partial \Phi_j^D}{\partial R} - ik\Phi_j^D\right) = 0 \tag{8}$$

(2) Radiation wave

Free surface conditions:

$$\frac{\partial^2 \Phi_j^R}{\partial n} = -\frac{\omega^2}{g}\Phi_j^R \; z = 0 \tag{9}$$

Object surface conditions:

$$\left.\frac{\partial \Phi_j^R}{\partial n}\right|_S = n_j \tag{10}$$

Seabed boundary conditions:

$$\left.\frac{\partial \Phi_j^R}{\partial n}\right|_{z=-h} = 0 \tag{11}$$

Infinite condition:

$$\lim_{R\to\infty} \sqrt{R}\left(\frac{\partial \Phi}{\partial R} - ik\Phi\right) = 0 \tag{12}$$

3. Development of Initial Model

In this study, a response surface optimization design method, incorporating the response surface model and gradient descent algorithm, is employed to optimize an A-type floating body. First, a parametric model was developed based on the initial model with predefined boundary conditions, and the finite element analysis was conducted. Moreover, the PB (Plackett–Burman) and CCD (Central Composite Design) tests were performed to analyze the parameter sensitivity of the model variables and to establish the response surface mode. The response surface equation was then optimized using the gradient descent method. Finally, the optimized model was verified under extreme conditions. The specific operation process is illustrated in Figure 1. The follow-up sections in this chapter describe the development of the initial model and stress strength analysis.

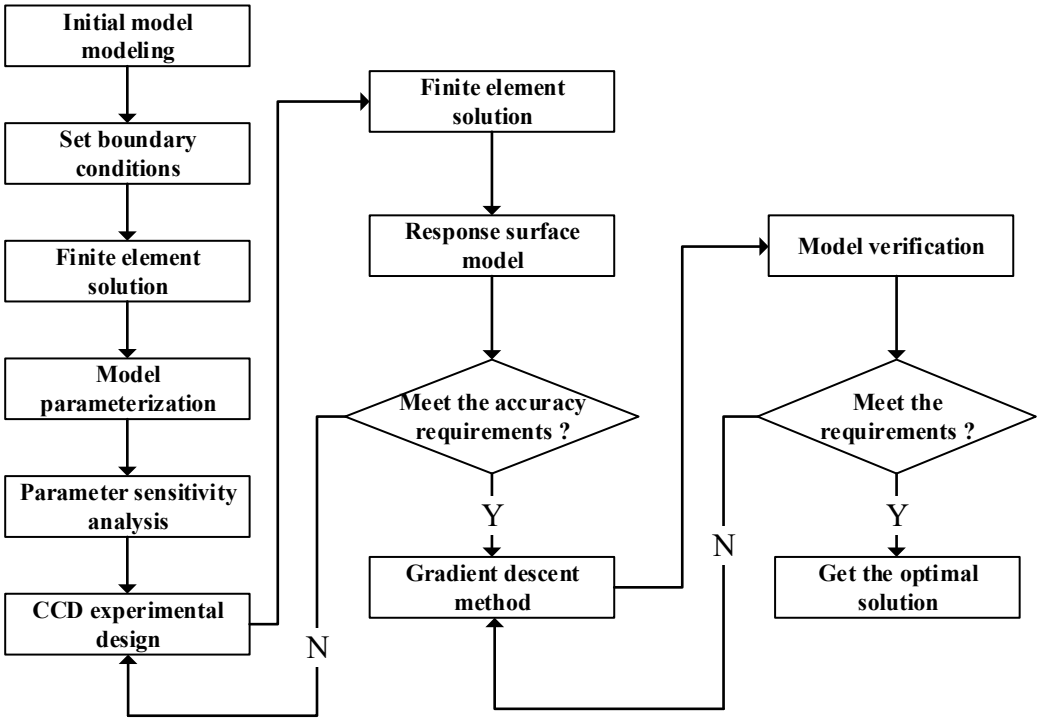

Figure 1. Optimized design process.

3.1. Structural Parameters of Initial Model

The FOWT platform primarily consists of buoy columns, heave plates, pontoons, and diagonal and transverse braces, arranged in a triangular configuration. The wind turbine tower is set at the top of one of the three columns, while the ballast tank and empty cabin are set inside the buoy column, heave plate, and pontoon to maintain the equilibrium between the platform's overall gravity and buoyancy of the platform. The main parameters of the model and the schematic diagram of the model are presented in Table 1 and Figure 2, respectively.

Table 1. Main parameters of FOWT.

Parameter of Model	Value
Water depth	100 m
Center of gravity	(0 m, 0 m, −7.2 m)
Platform mass	6035 t
Draft of platform	25 m
Ballast water density	1025 kg/m^3

The numerical simulation of the floating platform structure was performed in SESAM 2021 [24], a specialized software developed by Det Norske Veritas (DNV) (Oslo, Norway) for the design, analysis, and evaluation of marine engineering and offshore structures. Specifically, the structural model was established using GeniE 2021 and the strength analysis of local structure was carried out in Sestra 2021, which are both modules incorporated in the SESAM software 2021. Additionally, the pontoon is divided into six sections, numbered 1~6 from bottom to top. The thickness distribution of the bulkhead and the arrangement of the internal stiffener are shown in Figures 3 and 4, respectively.

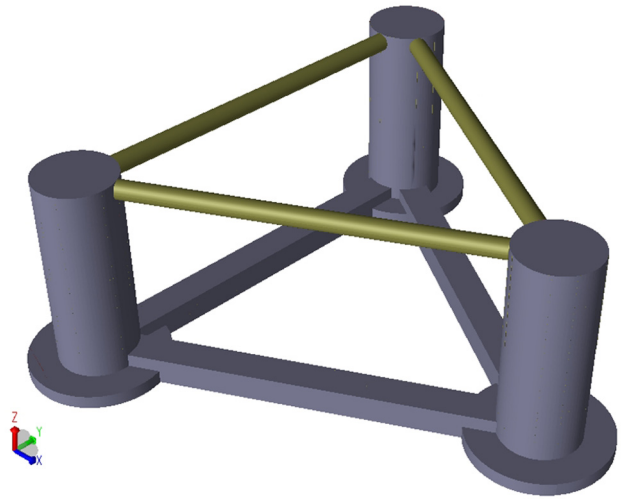

Figure 2. Appearance of newly designed FOWT.

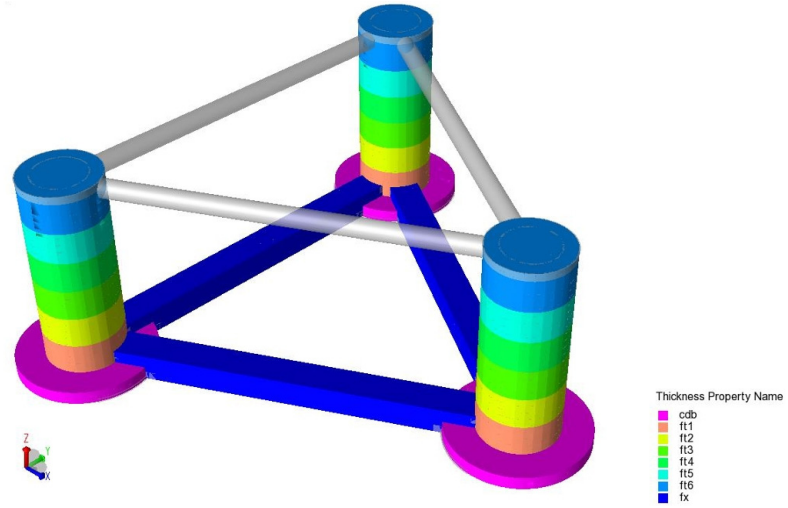

Figure 3. Bulkhead thickness distribution map.

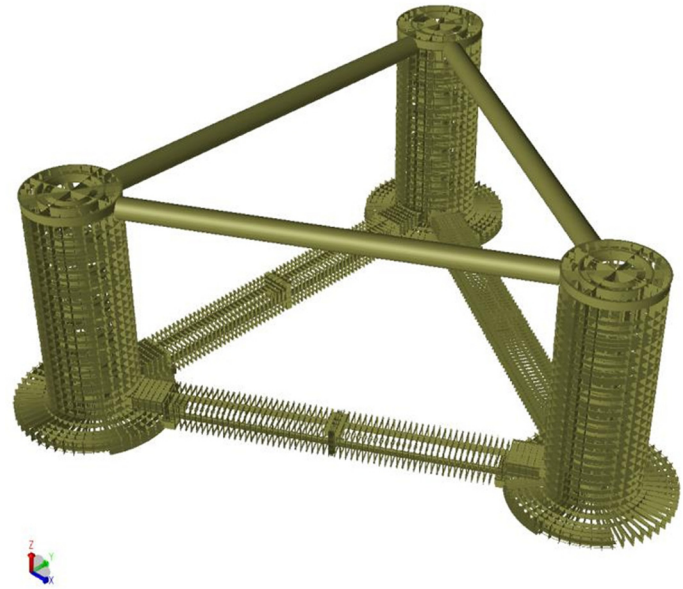

Figure 4. Layout diagram of stiffening rib.

3.2. Marine Environmental Conditions

For the strength study of the platform structure, the hydrostatic pressure, structural weight, wind load, and wave load are considered, which are applied to the floating platform by linear superposition through multiplication with their respective sub-coefficients [23], and the load sub-coefficients are shown in Table 2.

Table 2. Partial safety factors for loads.

Design Load	Wave Load	Wind Load	Hydrostatic Pressure	Structural Weight
Coefficients	1.3	1.3	1.0	1.0

(1) Wind load distributed on the wind turbine tower

The wind load can be calculated by the horizontal wind force from Equation (2), which takes into account wind speed, structural body type coefficient, air density, windward area, and other factors to accurately determine the magnitude of the load exerted by the wind on the structure. Herein, the limit state of wind load is considered with a wind speed of 51.5 m/s. The distributions of wind loads acting along the height of the tower, as well as the total load on the blades, is provided in Table 3.

Table 3. Wind load distributed along the height of wind turbine tower.

Loading Positions (m)	Wind Thrust Force (N)
29.75	45,529.12
40.25	62,669.36
51.75	69,545.74
63.25	74,016.26
74.75	73,998.12
86.25	76,616.77
97.75	78,147.65
109.57	82,906.32
119 m (Height of rotor center)	1,450,000

(2) Wave conditions under the most unfavorable conditions

Long-term forecast design wave method is a commonly used method in the field of marine and shipbuilding engineering. It is mainly based on spectral analysis to forecast ship profile wave load, statistically characterizing its frequency response function and long-term distribution. It can determine the design wave parameters, such as wave height, period, direction, etc., providing a basis for the design of the floating platform structure and the strength assessment in order to more realistically reflect the actual wave loading condition [25].

The calculation of wave loads on marine structures can generally be judged according to the ratio of the characteristic size D and wavelength λ. For large-size components ($D/\lambda > 0.15$), the wave loads were mainly calculated using the potential flow theory. Based on the wave direction, wave height, and period tabulated in Table 4, the velocity potential was determined according to Laplace's equation and the boundary conditions of free surface, object surface, and the seabed. Then, Bernoulli's equation was employed to calculate the fluid pressure, and finally, the wave load was obtained by integrating the pressure on the surface of the structure [26]. In addition, the hydrostatic pressure and structural weight were easily obtained according to the principles of hydrostatics and Newton's second law, respectively.

Table 4. Design wave for strength calculation.

Condition Number	Direction (°)	Amplitude (m)	Period (s)
LC1	0	8.17	6.8
LC2	0	6.46	9.6
LC3	0	6.96	10
LC4	0	8.17	19
LC5	75	8.05	7.2
LC6	90	7.87	25
LC7	90	8.05	27
LC8	105	8.05	7.2
LC9	180	6.46	9.6
LC10	180	6.96	10
LC11	180	8.17	19
LC12	270	7.87	25
LC13	270	8.05	27

3.3. Establishment of Finite Element Model

(1) Setting boundary conditions

In order to make up for the limitation that mooring system cannot be set directly on the platform in GeniE software 2021, equivalent boundary conditions were adopted to simulate the mooring effect [25], as shown in Figure 5. Regarding the translational degrees of freedom at the center point of heave columns, the first point (SP1) is constrained in the X-, Y- and Z-axis directions; the second point (SP2) is restricted along Y- and Z-axis directions; and the third point (SP3) is limited only in the Z-axis direction [27].

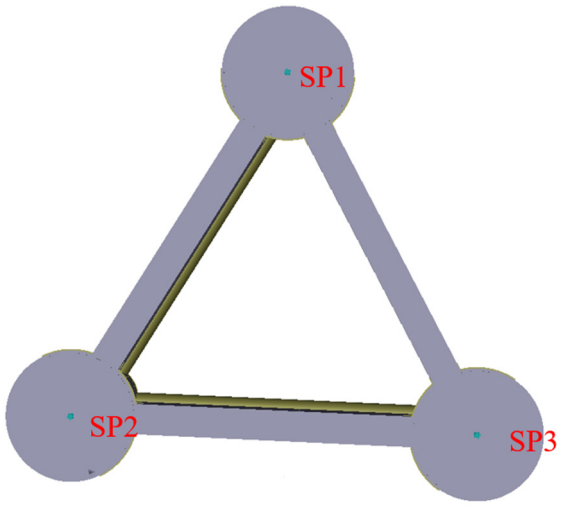

Figure 5. Model boundary condition.

(2) Finite element model

Based on the structural parameters of the floating platform, the initial model was established in GeniE software, consisting of components such as buoy, pontoon, heave plate, diagonal brace, and transverse brace. To accurately represent the real properties of the structure, the buoy, pontoon, heave plate, bulkhead, and rib plate were modeled as plate elements, while the diagonal brace, transverse brace, and internal skeleton were constructed using beam elements. Additionally, the interior was separated by ribs, and the overall strength of the model was ensured by the steel structure framework. This finite element model was meshed with a size of 2 m, as shown in Figure 6.

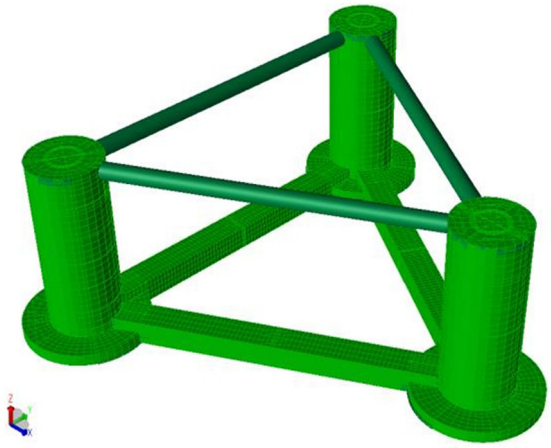

Figure 6. Finite element model of floating offshore wind turbine platform.

3.4. Stress Calculation of Initial Structure Model

According to DNV GL-OS-C103 [27], the structural design should satisfy the strength requirement below the material yield stress with a proper safety factor. In this study, Q355 steel, which exhibits a yield strength of 355 MPa, was employed. After taking into account a safety factor of 1.25, the structural stresses were required to remain below 284 MPa. The results of the structural strength assessment under 13 conditions are listed, and all cases satisfy the required specifications. Based on this validated initial model, structural optimization was subsequently carried out.

4. Response Surface Optimization

The response surface method employed in this study is a widely used optimization technique that constructs a mathematical model to describe the relationship between parameters and response variables. This is achieved by fitting regression equations based on a set of sample points generated through orthogonal experimental design, and is applied to predict the optimal solution of the model under the set constraints [28]. The orthogonal design serves to reduce the number of tests required and improve optimization efficiency [29,30]. In this process, an orthogonal design table is used to disperse the variable values, ensuring a balanced exploration of the design space. Analysis of variance, regression analysis, model fitting, and optimization analysis were performed using Design Expert 2021, an experimental design software developed by Stat-Ease Inc. (Minneapolis, MN, USA) [31]. Design Expert mainly analyzes the data derived from SESAM 2021 where the results are imported into Design Expert, and the analysis of variance function of Design Expert is used to evaluate the effects of different parameters on the structural performance. The mathematical relationship between the structural response and the parameters is explored with the help of regression analysis in order to construct an accurate regression model, and optimization analyses are carried out in order to find the optimal solution for the structural design.

4.1. Mathematical Model for Response Surface Optimization

4.1.1. Design Variables

The floating platform is mainly divided into three parts, viz., pontoon, buoy, and heave plate. In the optimization process, the bulkhead thickness, stiffener spacing, and stiffener size of the above parts are parameterized, including a total of 10 variables. The correspondence between variables and structural dimensions, as well as the designed variable value, are shown in Table 5. Therefore, the new floating body structure can be constructed by combining the changed variable. That is, the design variable is:

$$X = (A, B, C, D, E, F, G, H, I, J)^T \quad (13)$$

Table 5. Parametric modeling variable design table.

Variable Number	Variable Name	Variable Value
A	Bulkhead thickness of buoy for 1~6 sections (Figure 3)	0.018 m, 0.016 m, 0.016 m, 0.016 m, 0.016 m, 0.016 m
B	Bulkhead thickness of heave plate	0.019 m
C	Bulkhead thickness of pontoon	0.010 m
D	Spacing between pontoon longitudinal stiffener	12.8°
E	Number of transverse stiffeners in buoy	22
F	Size of float stiffener	height = 1 m, web thickness = 0.015 m, width = 0.3 m, top flange thickness = 0.015 m
G	Spacing between heave plate stiffener	7°
H	Size of heave plate stiffener size	height = 0.7 m, web thickness = 0.01 m, width = 0.2 m, top flange thickness = 0.01 m
I	Number of transverse stiffeners in pontoon	54
J	Size of pontoon transverse stiffener	height = 0.035 m, web thickness = 0.01 m, width = 0.2 m, top flange thickness = 0.01 m

4.1.2. Objective Function

The objective of this optimization design is to optimize the local structure of the floating platform by searching for the minimum solution of structural stress, i.e., the minimum value of $f(X)$, where $f(X)$ is obtained by the experimental design software, Design Expert software, based on the results of orthogonal tests. In summary, the optimized mathematical model is:

$$\begin{gathered} X = (A, B, C, D, E, F, G, H, I, J)^T \\ Minf(X) \\ s.t.(Mass)_L \leq Mass \leq (Mass)_U \\ s.t.(COMz)_L \leq COMz \leq (COMz)_U \end{gathered} \tag{14}$$

where $(Mass)_L$ and $(Mass)_U$ are the lower and upper limit of platform mass; and $(COMz)_L$ and $(COMz)_U$ are the lower and upper limit of platform center of mass, respectively.

The optimization of floating platform involves two key steps. The first step is concerned with the hydrodynamic optimization of the overall structure. This optimization requires the precise determination of key parameters such as mass, center of gravity, moment of inertia, and main scale. The goal of this optimization is to design a floating platform with excellent hydrodynamic characteristics and lower steel consumption, the detailed description of which referring to the reference [32] published by our group recently. These optimized parameters will provide a solid foundation for subsequent work.

The second step, viz., the current research work, involves optimizing the local structural strength. In the local structural optimization process, the thickness of internal reinforcement, the size of steel bars, and the layout of compartments are used as optimization variables. Due to practical constraints, it is difficult for the locally optimized model to correspond precisely to the parameters of the initial model. Herein, the constraints for the second step of local structural optimization are set to keep the variation of structural parameters (mass, center of mass) within ±5%, based on an in-depth study of the hydrodynamic performance of the floating body. Within this tolerance (±5%), the impact on the hydrodynamic performance of the floating body is negligible, and at the same time, sufficient space is provided for the optimization of the local structural dimensions [32].

4.2. Plackett–Burman Test

The significant factor is determined by executing the Plackett–Burman test, viz., comparing the difference between the two levels of each factor and the overall difference and conducting the parameter sensitivity analysis of the variables with the least number of tests [33]. The orthogonal test with n = 12 (Number of tests) is designed by investigating the 10 variables and defining the maximum stress value as the response value. The factor level and coded value of Plackett–Burman design are presented in Table 6, where variables A, B,

C, F, H, and J are all expressed in the form of variation coefficient to reflect the variation visually, viz., the ratio of changed size to initial size.

Table 6. Plackett–Burman design factor level and coding value.

Test Number	Variable Number									
	A	**B**	**C**	**D**	**E**	**F**	**G**	**H**	**I**	**J**
Lower limit	0.9	0.9	0.9	19	5	0.9	6	0.9	25	0.9
Upper limit	1.1	1.1	1.1	23	9	1.1	8	1.1	29	1.1

After orthogonal tests, the distribution of the maximum and minimum stress results is shown in Figure 7. It is obvious that LC4 and LC11 are the most unfavorable among the 13 working conditions, thus the subsequent analysis should focus on these two conditions.

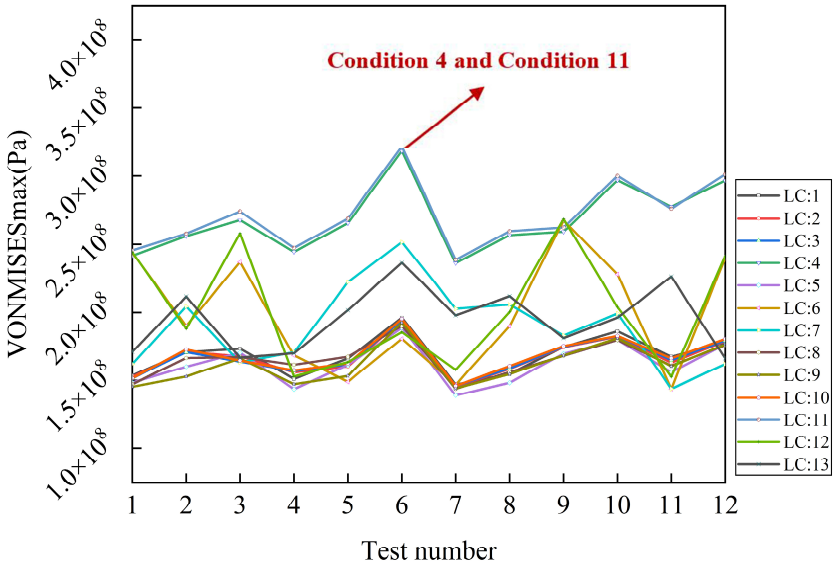

Figure 7. Plackett–Burman test results distribution.

The F-value is a crucial statistical metric in regression analysis, which is usually employed to evaluate whether the model as a whole is statistically significant. Specifically, if the computed F-value is large and the corresponding p-value, derived from the F-distribution, is less than the pre-established significance level of $\alpha = 0.05$, it indicates that the model is significant. In this context, by comparing the magnitudes of the F-values of different variables, the relative importance or significance of these variables can be ranked. The higher the F-value of a variable, the more significant its contribution to the model. The R^2 and R^2_{adj} are important indicators of closeness of the linear relationship between multiple independent variables and a dependent variable, where an absolute value closer to 1 indicates a stronger linear relationship between the independent variables and the dependent one. In regression analysis, R^2 rises with the increasing number of independent variables, even if the new independent variables have no substantial explanatory significance to the dependent variable, which may induce misjudgment. However, the R^2_{adj} can make up for this shortcoming by taking into account the number of independent variables and the sample size, making the assessment of goodness of fit more objective and precise, which provides a reliable basis for choosing the reliable model and judging the validity of independent variables. Below are the formulas for R^2 and R^2_{adj} [34]:

$$f(X) = \beta_0 + \beta_1 X_1 + \beta_2 X_2 + \ldots + \beta_k X_k + \epsilon \quad (15)$$

$$SST = \sum_{i=1}^{n} \left(f(X_i) - \overline{f(X)} \right)^2 \tag{16}$$

$$SSR = \sum_{i=1}^{n} \left(\hat{f}(X_i) - \overline{f(X)} \right)^2 \tag{17}$$

$$R^2 = SSR/SST \tag{18}$$

$$R^2_{adj} = 1 - (1 - R^2) \frac{n-1}{n-j-1} \tag{19}$$

where X_1, X_2, …, X_k are the independent variables, β_0, β_1, …, β_k are the regression coefficients, ε is the random error, SST is the sum of squared total deviations, SSR is the computed sum of squared regressions where n is the number of samples, $f(X_i)$ is the i−th observation, $\overline{f(X)}$ is the sample mean of $f(X)$, $\hat{f}(X_i)$ is the ith observation predicted by the regression model, and j is the number of independent variables.

From Table 7, the order of magnitude of the F-values shows that the variable significance of the condition 4 model meets the requirements (B > J > H > C > E > D > A > F > G > I). The model correlation coefficient R^2 is 0.9155 determining an excellent model correlation. The correction coefficient R^2_{adj} is 0.8672, viz., the model can explain more than 86.72% of the response value changes. Table 8 shows that the p-value of the model under LC11 is 0.0682 more than 0.05, illustrating the model does not fit well in the regression area in this study, which is led by too many unrelated factors the model contains. Therefore, the variance analysis of the model was performed again after removing the irrelevant factors, as shown in Table 9. According to the F-value, the degree of influence is sorted: J > B > H > C > E > D > F > A > I > G. In this case, it is found that the model correlation coefficient R^2 is 0.9150, indicating a high model correlation, and the correction coefficient R^2_{adj} is 0.8665, meaning the model can explain more than 86.65% of the response value changes.

The results of the Plackett–Burman test are identified by the Lenth method [35]. The semi-normal probability of the standardized effects for LC4 and LC11 are obtained as shown in Figure 8. It is found that the standardized effect points of factors B, C, H, and J are far from the fitting point, which means the thickness of the heave plate and pontoon bulkhead as well as the size of the heave plate and pontoon stiffener are the four factors affecting the maximum stress. According to the Pareto diagram of the standardized effects of factors as shown in Figure 9, it can be seen that the t-value of the statistical test for factors B, C, H, and J exceeds the limit for determining the significance of the factors; therefore, these factors can be further proved to be significant factors.

Table 7. Significance analysis of condition 4 results.

Source	Sum of Squares	Degree of Freedom	Mean Square	F	p	Significant
Model	6.905×10^{15}	10	6.905×10^{14}	289.45	0.0457	Yes
A	4.481×10^{13}	1	4.481×10^{13}	18.78	0.1444	No
B	2.084×10^{15}	1	2.084×10^{15}	873.46	0.0215	Yes
C	9.426×10^{14}	1	9.426×10^{14}	395.10	0.0320	Yes
D	1.684×10^{14}	1	1.684×10^{14}	70.58	0.0754	No
E	3.057×10^{14}	1	3.057×10^{14}	128.13	0.0561	No
F	4.470×10^{13}	1	4.470×10^{13}	18.74	0.1445	Yes
G	1.140×10^{13}	1	1.140×10^{13}	4.78	0.2731	No
H	1.323×10^{15}	1	1.323×10^{15}	554.57	0.0270	Yes
I	6.278×10^{12}	1	6.278×10^{12}	2.63	0.3517	No
J	1.975×10^{15}	1	1.975×10^{15}	827.71	0.0221	Yes
Residual	2.386×10^{12}	1	2.386×10^{12}	—	—	—
Cor Total	6.908×10^{15}	11	—	—	—	—

Table 8. Significance analysis of condition 11 results.

Source	Sum of Squares	Degree of Freedom	Mean Square	F	*p*	Significant
Model	6.994×10^{15}	10	6.994×10^{14}	129.89	0.0682	No
A	8.128×10^{13}	1	8.128×10^{13}	15.09	0.1604	No
B	1.988×10^{15}	1	1.988×10^{15}	369.12	0.0331	Yes
C	1.037×10^{15}	1	1.037×10^{15}	192.50	0.0458	Yes
D	1.484×10^{14}	1	1.484×10^{14}	27.56	0.1198	No
E	2.251×10^{14}	1	2.251×10^{14}	41.79	0.0977	No
F	8.338×10^{13}	1	8.338×10^{13}	15.48	0.1584	No
G	1.571×10^{13}	1	1.571×10^{13}	2.92	0.3372	No
H	1.355×10^{15}	1	1.355×10^{15}	251.61	0.0401	Yes
I	3.555×10^{13}	1	3.555×10^{13}	6.60	0.2363	No
J	2.026×10^{15}	1	2.026×10^{15}	376.25	0.0328	Yes
Residual	5.385×10^{12}	1	5.385×10^{12}	—	—	—
Cor Total	7.000×10^{15}	11	—	—	—	—

Table 9. Significance analysis of condition 11 results (after correction).

Source	Sum of Squares	Degree of Freedom	Mean Square	F	*p*	Significant
Model	6.979×10^{15}	9	7.754×10^{14}	73.52	0.0135	Yes
A	8.128×10^{13}	1	8.128×10^{13}	7.71	0.1090	No
B	1.988×10^{15}	1	1.988×10^{15}	188.47	0.0053	Yes
C	1.037×10^{15}	1	1.037×10^{15}	98.29	0.0100	Yes
D	1.484×10^{14}	1	1.484×10^{14}	14.07	0.0643	No
E	2.251×10^{14}	1	2.251×10^{14}	21.34	0.0438	Yes
F	8.338×10^{13}	1	8.338×10^{13}	7.91	0.1066	No
H	1.355×10^{15}	1	1.355×10^{15}	128.46	0.0077	Yes
I	3.555×10^{13}	1	3.555×10^{13}	3.37	0.2078	No
J	2.026×10^{15}	1	2.026×10^{15}	192.10	0.0052	Yes
Residual	2.109×10^{13}	2	1.055×10^{13}	—	—	—
Cor Total	7.000×10^{15}	11	—	—	—	—

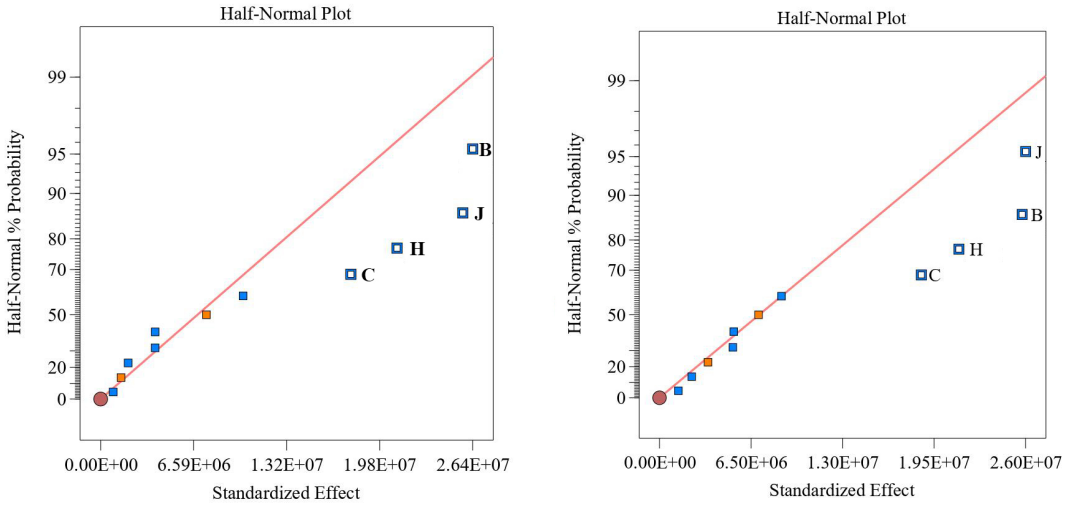

Figure 8. Half-normal plot of stress results under condition 4 (**left**) and condition 11 (**right**).

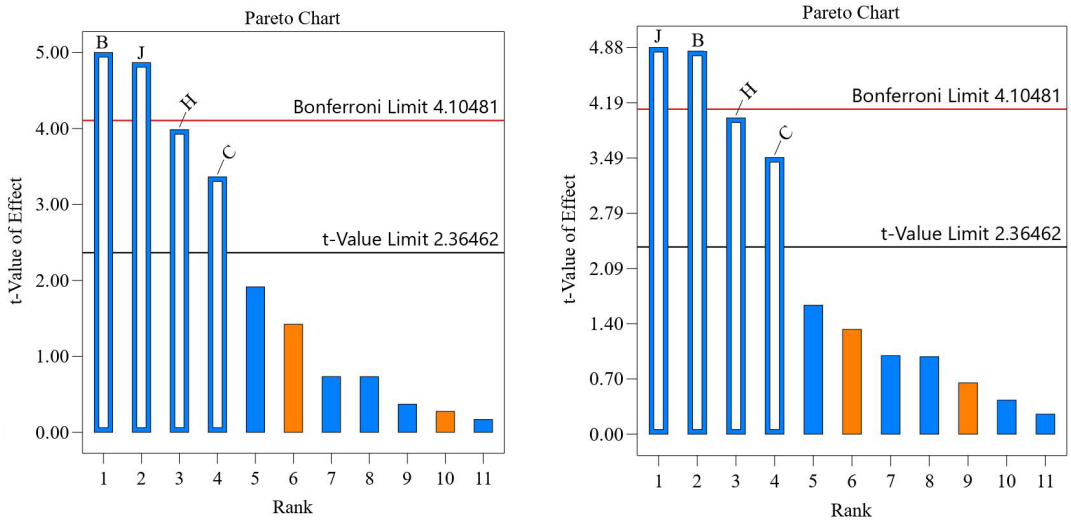

Figure 9. Normalized effect Pareto diagram of stress results under condition 4 (**left**) and condition 11 (**right**).

Overall, too many variables in the response surface analysis might lead to the response surface model being inaccurate [36]. Therefore, only the top four variables with greater influence were retained, including the thickness of the heave plate and pontoon bulkhead as well as the size of the heave plate and pontoon stiffener.

4.3. Response Surface Analysis (Central Composite Design)

Based on the conclusion of the previous subsection, four variables were selected for the Central Composite Design test [37,38], including the thickness of the heave plate bulkhead, the thickness of the pontoon bulkhead, the size of the heave plate stiffener, and the size of the pontoon stiffener, which were relabeled as A, B, C, and D, respectively. By setting the parameter range and interval to 0.8~1.2 and 0.025, respectively, a total of 332 combinations of orthogonal test combinations were obtained. The stress maximum value, mass, and centroid position were taken as the response values in the test, and the ultimate goal was to obtain the smallest maximum stress value under each working condition. Meanwhile, the parameter ranges of mass and centroid were kept within ±5% of the initial model parameters as shown in Figure 10. Table 10 shows that the experimental design factor level and coded value.

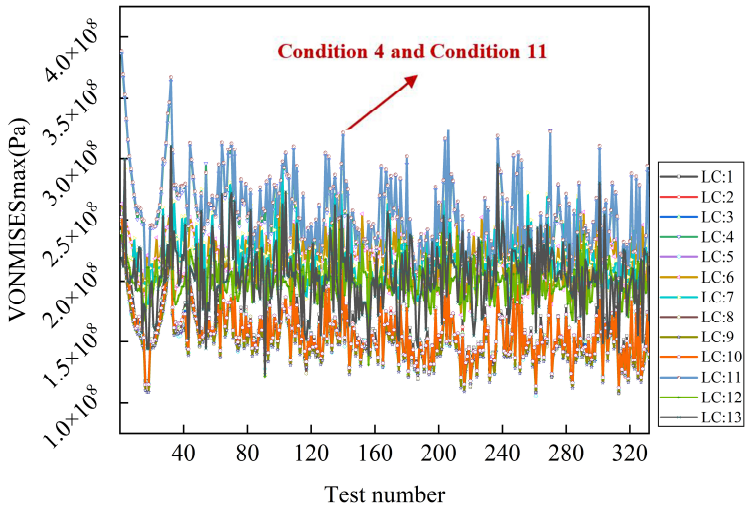

Figure 10. Central Composite Design test results distribution diagram.

Table 10. Central Composite Design factor levels and coded values.

Test Number	Variable Number			
	A	**B**	**C**	**D**
Lower limit	0.800	0.800	0.800	0.800
Upper limit	1.200	1.200	1.200	1.200

The results obtained by significance analysis of the model are shown in Table 11. It is observed that the four response value models of the von Mises stress under LC4 and LC 11, as well as the mass and the center of mass, are extremely significant ($p < 0.05$). As shown in Table 12, the model correlation coefficient R^2 and the correction coefficient R^2_{adj} are all above 0.98 with an excellent model fitting degree, where R^2_{adj} means all models can explain more than 98% of the response value changes. Therefore, each regression model can be used to analyze and predict the above-mentioned four response value models (A, B, C, D).

Table 11. Results obtained by model significance analysis.

Model	Degree of Freedom	Sum of Squares	Mean Square	F	*p*	Significant
von Mises stress (LC 4)	3.329×10^{17}	14	2.378×10^{16}	1541.21	<0.001	Yes
von Mises stress (LC 11)	3.318×10^{17}	14	2.370×10^{16}	1331.08	<0.001	Yes
Mass	6.353×10^{12}	14	4.538×10^{11}	4.04×10^{10}	<0.001	Yes
COMz	42.98	14	3.07	1.03×10^{7}	<0.001	Yes

Table 12. Model correlation coefficient and correction coefficient.

Model	R^2	R^2_{adj}
von Mises stress (LC 4)	0.9855	0.9894
von Mises stress (LC 11)	0.9833	0.9825
Mass	0.9999	0.9999
COMz	0.9999	0.9999

Based on the obtained regression model, the error distribution of the value predicted by the model and the correlation between the predicted and experimental value are shown in Figure 11. To better evaluate the model, an index, the prediction errors not exceeding ±2 SD (standard deviation), is defined as a criterion for excellent prediction model. According to the error distribution maps of the four models in Figure 11a,c,e,g, the sample prediction error values are within ±2 SDs (standard deviations), while no anomalous sample points indicate the high prediction accuracy of the model. From the correlation diagram of the model predicted value and the experimental value in Figure 11b,d,f,h, it is obvious that the sample points are all near the 45° diagonal with a small difference, which indicates a high goodness fit between predicted and experimental values.

The change range of the limiting mass and centroid is selected to be ±4% for predicting the minimum stress in the feasible region. Meanwhile, the A variable (heave plate bulkhead thickness) and C variable (heave plate stiffener size) are adjusted to 0.8~1.4 and 0.7~1.2, respectively, to make the variable prediction point fall within the variable range, as shown in Table 13.

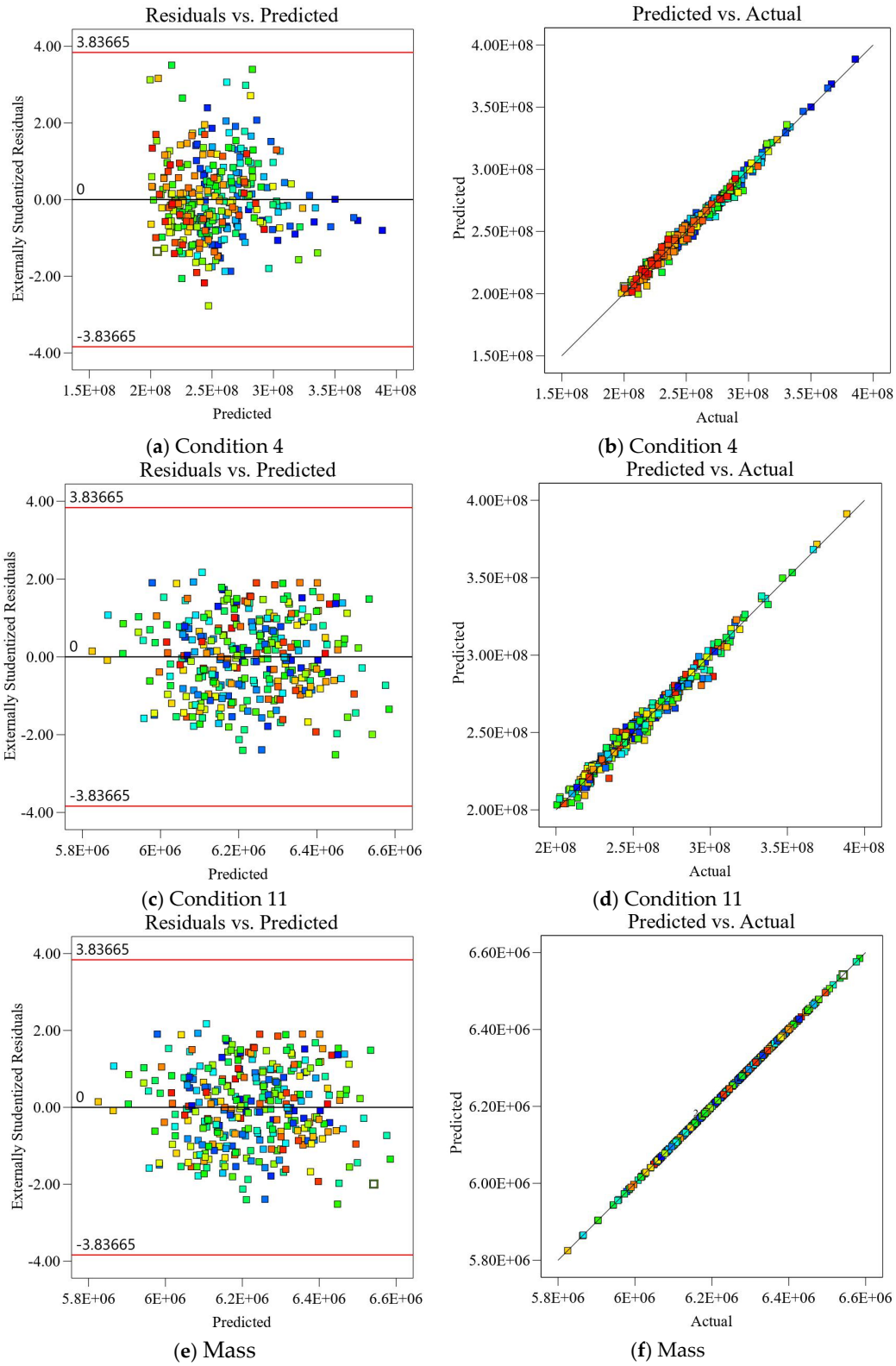

(**a**) Condition 4 (**b**) Condition 4

(**c**) Condition 11 (**d**) Condition 11

(**e**) Mass (**f**) Mass

Figure 11. *Cont*.

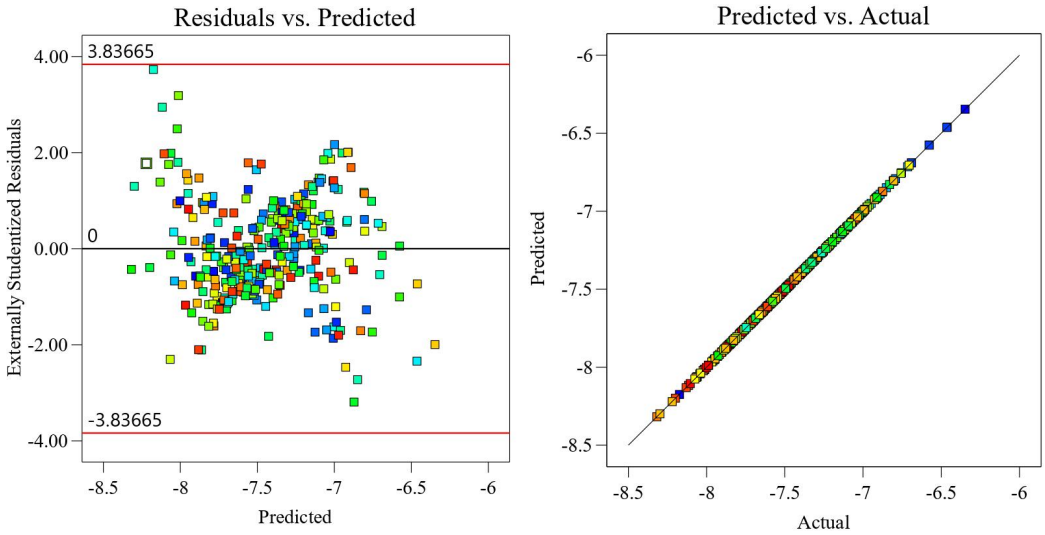

(**g**) COMz (**h**) COMz

Figure 11. Prediction error distribution diagram (**a**,**c**,**e**,**g**) and correlation diagram between predicted value and experimental value (**b**,**d**,**f**,**h**).

Table 13. Estimation range.

Name	Goal	Lower Limit for LC4	Upper Limit for LC4	Lower Limit for LC11	Upper Limit for LC11
A	In range	0.8	1.4	0.8	1.4
B	In range	0.8	1.2	0.8	1.2
C	In range	0.7	1.2	0.7	1.2
D	In range	0.8	1.2	0.8	1.2
von Mises stress	Minimize and in range	1.98×10^8	3.86×10^8	1.98×10^8	3.86×10^8
Mass	In range	5.80×10^6	6.28×10^6	5.80×10^6	6.28×10^6
COMz	In range	−7.488	−6.912	−7.488	−6.912

The response surface diagram of the maximum von Mises stress value, mass, and centroid position within the prediction range under LC4 and LC11 are presented in Figures 12 and 13, respectively. The feasible region for minimum solution of the maximum stress value is determined by the boundaries of the limit mass and centroid position. In Figure 12, the predictions for mass and centroid position based on the response surface model under LC4 remain within the allowable limits. The minimum solution of the predicted von Mises stress maximum value is 2.21×10^8 Pa, with the credibility being as high as 0.88.

In Figure 13, it is found that the mass and COMz predicted by the response surface model under LC11 remain within the allowable range, where the minimum solution of the largest predicted von Mises stress value is 2.23×10^8 Pa, whose credibility value is 0.882 with a fine predicted feasibility. Moreover, the variable values can be roughly estimated, thanks to the optimal value prediction point in the response surface model falls within the range of the four variables; subsequently, the response surface equation needs to be solved by using a numerical calculation method to determine the specific variable value.

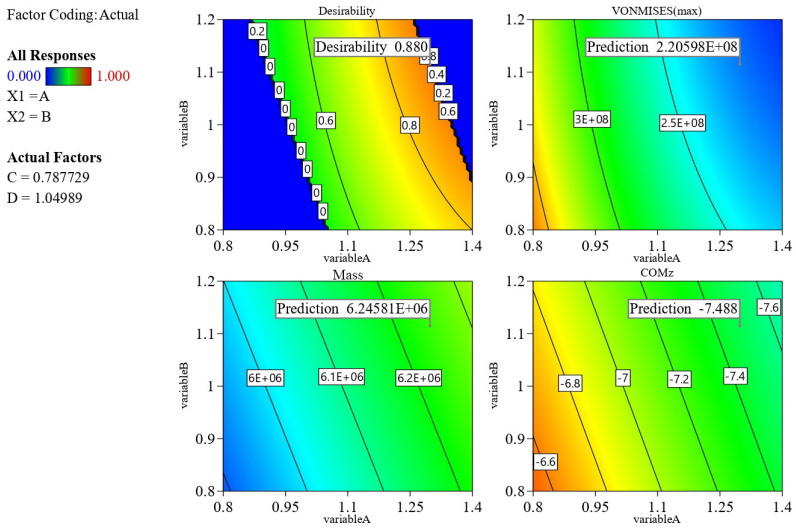

(**a**) Interaction between factor A and factor B.

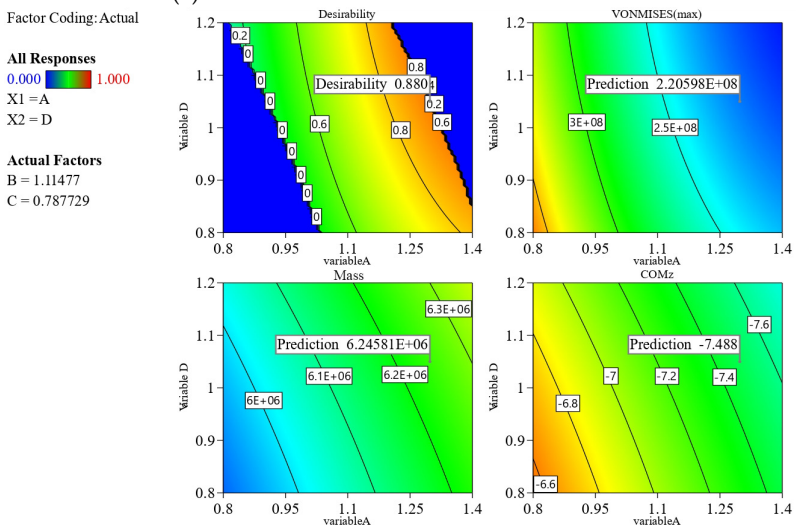

(**b**) Interaction between factor A and factor D.

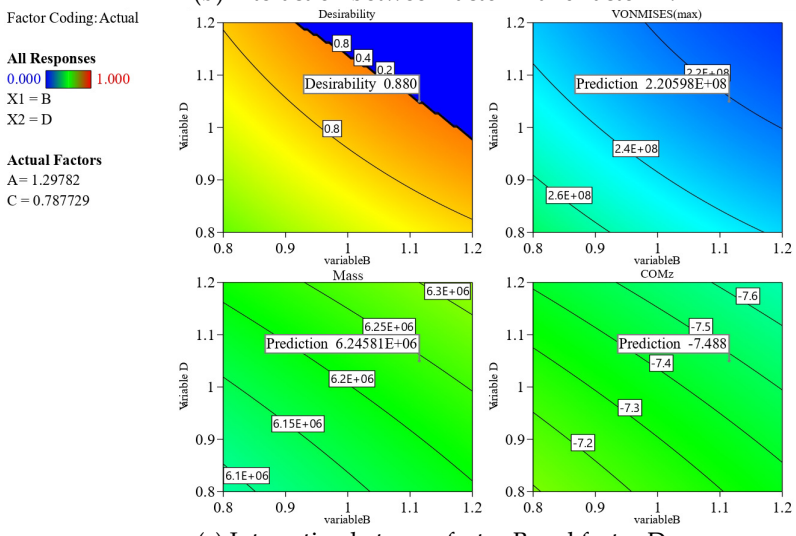

(**c**) Interaction between factor B and factor D.

Figure 12. *Cont*.

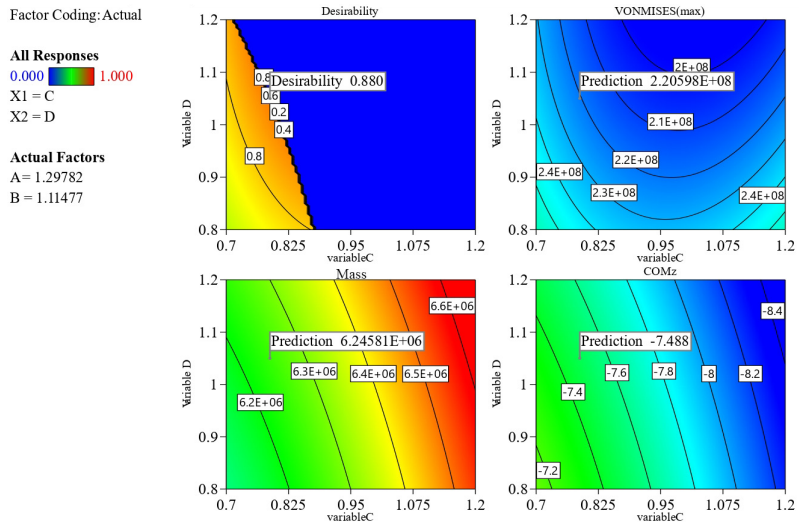

(**d**) Interaction between factor C and factor D.

Figure 12. Response surface model under LC4.

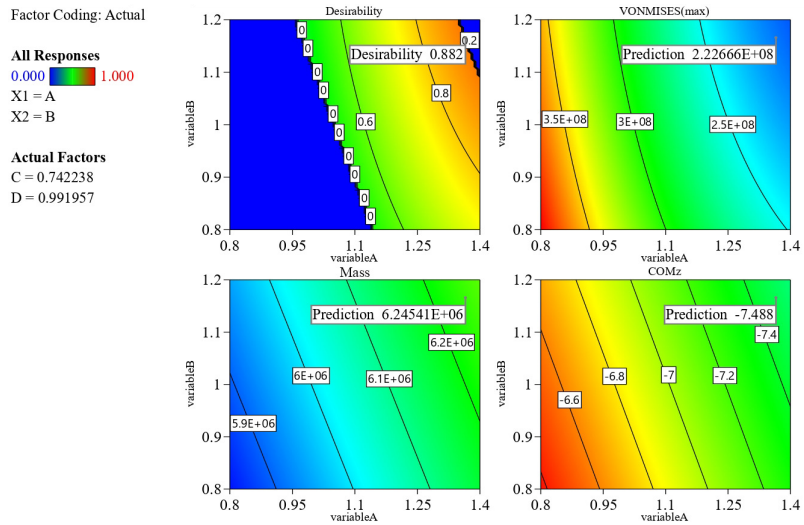

(**a**) Interaction between factor A and factor B.

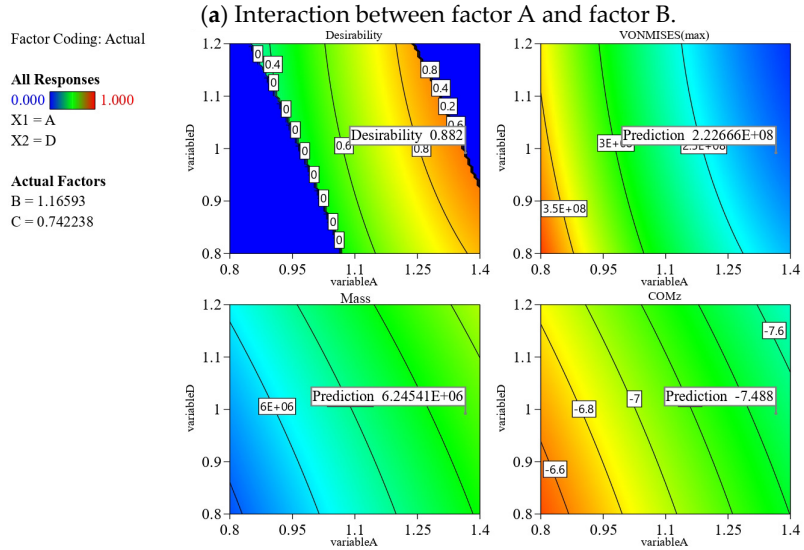

(**b**) Interaction between factor A and factor D.

Figure 13. *Cont*.

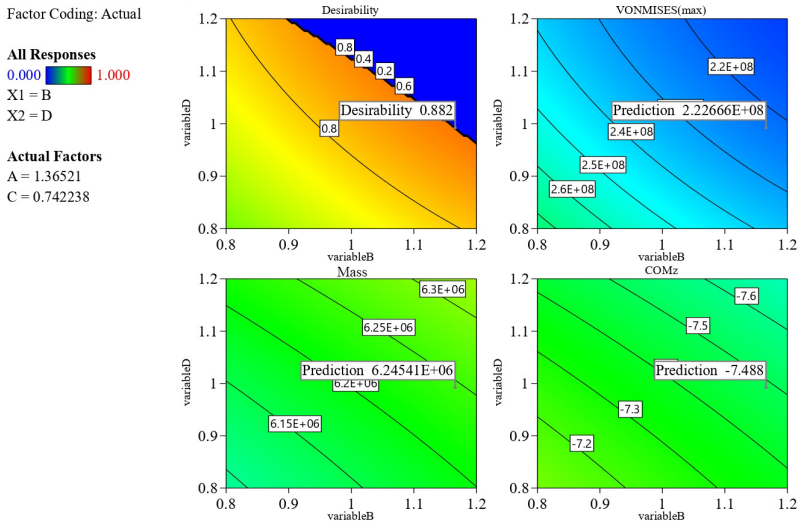

(**c**) Interaction between factor B and factor D.

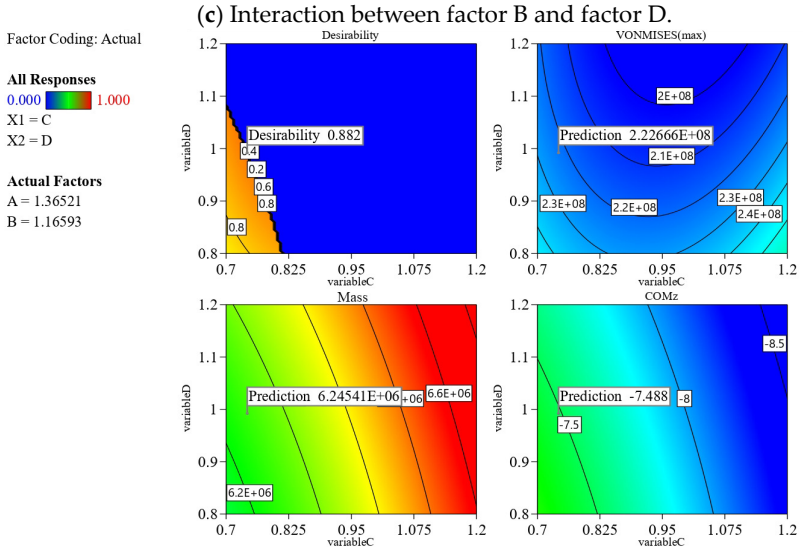

(**d**) Interaction between factor C and factor D.

Figure 13. Response surface model under LC11.

4.4. Gradient Descent Method Solution

The gradient descent method is a widely used numerical algorithm for solving the minimum value of the objective function. The optimization process begins at a random point and progresses toward the minimum value along the direction of the steepest descent defined by the objective function. To enhance robustness, the search process should initiate from multiple starting points within the design space. After a certain number of iterations, the optimal solution can be identified [39].

For the optimal targeting function $f(X_i)$, the update formula of the gradient descent method is as follows [40]:

$$X_{i+1} = X_i - \alpha \nabla f(X_i) \tag{20}$$

where X_{i+1} is the updated parameter vector, X_i is the current parameter vector, α is the learning rate, which is used to control the step size of the update, and $\nabla f(X_i)$ is the gradient of the objective function $f(X_i)$ at X_i.

Based on the response surface equations established in Section 4.3, the constraint conditions and optimization objectives are set up; subsequently, the optimal solution of the response surface model is obtained after 10,000 iterations. The optimization process and results are shown in Figure 14 and Table 14, respectively.

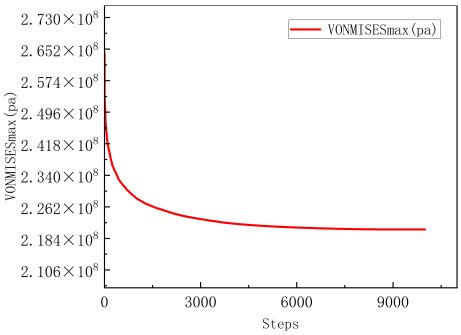

(**a**) Maximum stress under LC4.

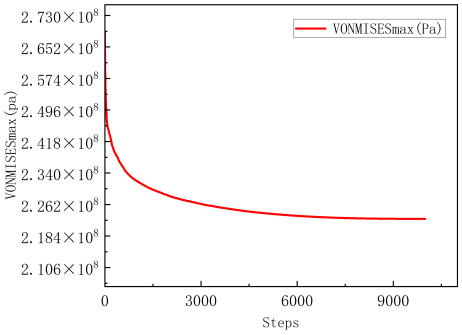

(**b**) Maximum stress under LC11.

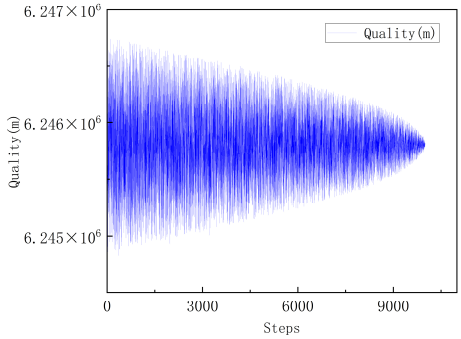

(**c**) Mass under LC4.

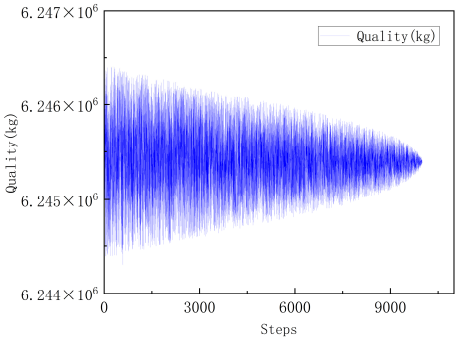

(**d**) Mass under LC11.

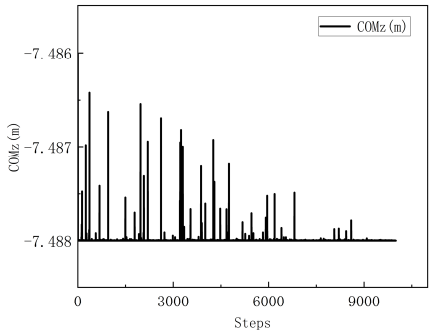

(**e**) Center of mass under LC4.

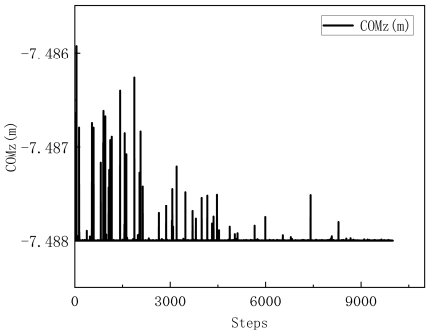

(**f**) Center of mass under LC11.

Figure 14. Gradient descent method solving process.

Table 14. Optimal results.

Loading Condition	Variable Number				Target Value		
	A	B	C	D	von Mises Stress (Pa)	Mass (kg)	COMz (m)
LC4	1.297	1.116	0.788	1.049	2.263×10^8	6.246×10^6	−7.488
LC11	1.365	1.163	0.742	0.995	2.260×10^8	6.245×10^6	−7.488

4.5. Results Verification

To verify the model obtained by the optimization process, a finite element model was established in GeniE software 2021 and imported into HydroD software 2021 for structural strength calculation.

The von Mises stress of the optimal model is shown in Table 14, where the predicted maximum structural von Mises stress under LC4 is 226.3 MPa, larger than 226 MPa of the case under LC11. Therefore, the predicted model for the case under LC11 is determined to

be the optimal solution. As shown in Table 15, the mass and centroid position are increased by 3.36% and 3.85%, respectively, which satisfies the requirement that the gap between the initial and optimized model is within ±5%. Moreover, the maximum von Mises stress value of the optimized model is reduced by 22.12% after optimization, achieving the purpose of improving the structural safety in this study.

Table 15. Comparison before and after optimization.

Variable	Name	Optimized Model Variable Values	Comparison
A	Bulkhead thickness of heave plate	0.0259 m	—
B	Bulkhead thickness of pontoon	0.01163 m	—
C	Size of heave plate stiffener	height = 0.5894 m, web thickness = 0.00842 m, width = 0.1684 m, top flange thickness = 0.00842 m	—
D	Size of pontoon transverse stiffener	height = 0.0348 m, web thickness = 0.00995 m, width = 0.199 m, top flange thickness = 0.00995 m	—
—	Mass	6.245×10^6 kg	3.36%
—	COMz	−7.48826 m	3.85%
—	von Mises stress	2.260×10^8 Pa	−22.12%

5. Conclusions

In this paper, the floating wind turbine platform is taken as the research object, the local structure is parametrically analyzed using the orthogonal test method to obtain the optimal arrangement, and the optimal results are verified in terms of strength. The following conclusions are obtained.

(1) The initial model of the structure is established in GeniE software 2021, which is mainly composed of pontoon, buoy, and heave plate. The mass of the initial model steel structure is 6035 t, and the coordinates of the center of mass position are (0, 0, −7.2 m). The maximum stress value of the initial model was calculated in Sestra software 2021 as 276 MPa.

(2) A total of 10 variables, namely bulkhead thickness, spacing of stiffener, and size of stiffener, were parameterized for the three parts of pontoon, buoy, and heave plate. A Plackett–Burman test was used to analyze the significance of the 10 variables, which were ranked according to the *p*-value. It was determined that the thickness of the heave plate and pontoon bulkhead, and the section size of heave plate and pontoon stiffener are the most important factors influencing the magnitude of the structural stress in the floating platform.

(3) The Central Composite Design method was used to further analyze the above four variables. A total of 332 orthogonal tests were established, the factor levels of the selected variables were in the range of 0.8~1.2, the stress maxima, mass, and center of mass were used as the objective functions, all response surface models had *p*-values less than 0.0001, and the model correlation coefficients and model correction coefficients were above 0.98. The response surface models can well predict the changes of the response values of the stress maximum, mass, and center of mass under various working conditions.

(4) Based on the gradient descent algorithm, the minimum solution of the stress maximum value was solved by controlling the function range of mass and center of mass. After optimization, the maximum von Mises stress of the model was reduced by 22.12% under extreme conditions, and the mass and center of mass were increased by 3.36% and 3.85%, respectively, which satisfies the requirement of not exceeding ±5% between the initial model and the optimized one, achieving the purpose of improving structural safety in this study.

Author Contributions: Conceptualization, M.H.; Methodology, Y.R., M.H. and J.W.; Software, Y.R., M.H., J.H. and J.W.; Validation, Y.R.; Formal analysis, Y.R., J.H. and L.Z.; Investigation, Y.R., M.H., J.H., S.L., L.Z., H.Z. and W.S.; Resources, J.H., J.W., S.L. and L.Z.; Data curation, J.H., J.W. and S.L.; Writing—original draft, Y.R. and M.H.; Writing—review & editing, H.Z. and W.S.; Supervision, H.Z.; Funding acquisition, W.S. All authors have read and agreed to the published version of the manuscript.

Funding: This work is financially supported by the China Renewable Energy Engineering Institute Research Program (ZS-KJSD-20230005). Their financial supports are gratefully acknowledged.

Data Availability Statement: The original contributions presented in this study are included in the article. Further inquiries can be directed to the corresponding author.

Conflicts of Interest: The authors declare no conflict of interest.

References

1. Wang, F.; Hao, J.; Li, S.; Ren, J.; Xie, Y.; Zhang, B. Key technology and development trend of floating offshore wind power. *Water Power* **2022**, *48*, 9–12+117.
2. Xia, Y. In 2023, global offshore wind power will add 10.8 GW of new installed capacity. *WIND Energy Mag.* **2024**, *27*, 42–44.
3. Liu, X.; Han, X.; Qin, M. Status of floating wind power technology and prospect of offshore wind power development in China. *China Offshore Oil Gas* **2024**, *36*, 233–242.
4. Wan, L.; Moan, T.; Gao, Z.; Shi, W. A review on the technical development of combined wind and wave energy conversion systems. *Energy* **2024**, *294*, 130885. [CrossRef]
5. Tian, X.; Sun, X.; Liu, G.; Xie, Y.; Chen, Y.; Wang, H. Multi-objective optimization of the hull form for the semi-submersible medical platform. *Ocean Eng.* **2021**, *230*, 109038. [CrossRef]
6. Yang, H.; Zhu, Y.; Lu, Q.; Zhang, J. Dynamic reliability based design optimization of the tripod sub-structure of offshore wind turbines. *Renew. Energy* **2015**, *78*, 16–25. [CrossRef]
7. Saeed, N.; Gong, J.; Wan, Y.; Long, K.; Saeed, A.; Mei, L.; Xiong, C.; Long, W.; Zhou, H.; Li, L. A novel design of multifunctional offshore floating platform structure based on topology optimization. *Eng. Struct.* **2024**, *306*, 117782. [CrossRef]
8. Chen, M.; Huang, W.; Liu, H.; Hallak, T.S.; Liu, S.; Yang, Y.; Tao, T.; Jiang, Y. A novel SPM wind-wave-aquaculture system: Concept design and fully coupled dynamic analysis. *Ocean Eng.* **2025**, *315*, 119798. [CrossRef]
9. Lu, F.; Long, K.; Zhang, C.; Zhang, J.; Tao, T. A novel design of the offshore wind turbine tripod structure using topology optimization methodology. *Ocean Eng* **2023**, *280*, 114607. [CrossRef]
10. Karimi, M.; Hall, M.; Buckham, B.; Crawford, C. A multi-objective design optimization approach for floating offshore wind turbine support structures. *J. Ocean Eng. Mar. Energy* **2017**, *3*, 69–87. [CrossRef]
11. Lee, J.C.; Shin, S.C.; Kim, S.Y. An optimal design of wind turbine and ship structure based on neuro-response surface method. *Int. J. Nav. Archit. Ocean. Eng.* **2015**, *7*, 750–769. [CrossRef]
12. Ferri, G.; Borri, C.; Marino, E. Substructure optimization of a 10MW floating wind turbine for installations in the Mediterranean Sea. *J. Phys. Conf. Ser.* **2024**, *2647*, 112011. [CrossRef]
13. Choi, E.; Han, C.; Kim, H.; Park, S. Optimal design of floating substructures for spar-type wind turbine systems. *Wind Struct.* **2014**, *18*, 253–265. [CrossRef]
14. Benifla, V.; Adam, F. Development of a genetic algorithm code for the design of cylindrical buoyancy bodies for floating offshore wind turbine substructures. *Energies* **2022**, *15*, 1181. [CrossRef]
15. Dou, S.; Pegalajar-Jurado, A.; Wang, S.; Bredmose, H.; Stolpe, M. Optimization of floating wind turbine support structures using frequency-domain analysis and analytical gradients. *J. Phys. Conf. Ser.* **2020**, *1618*, 042028. [CrossRef]
16. Leimeister, M.; Kolios, A.; Collu, M.; Thomas, P. Design optimization of the OC3 phase IV floating spar-buoy, based on global limit states. *Ocean Eng.* **2020**, *202*, 107186. [CrossRef]
17. Hall, M.; Buckham, B.; Crawford, C. Evolving Offshore Wind: A Genetic Algorithm-Based Support Structure Optimization Framework for Floating Wind Turbines. In Proceedings of the 2013 MTS/IEEE OCEANS-Bergen, Bergen, Norway, 10–14 June 2013.
18. Hegseth, J.M.; Bachynski, E.E.; Martins, J.R. Integrated design optimization of spar floating wind turbines. *Mar. Struct.* **2020**, *72*, 102771. [CrossRef]
19. Tang, Y.; Shen, G.; Liu, L. *Structural Dynamics of Ocean Engineering*; Tianjin University Press: Tianjin, China, 2008.
20. DNV GL. *Stability and Watertight Integrity: DNVGL-OS-C301*; DNV GL: Høvik, Norway, 2020.
21. Islam, M.T. Design, Numerical Modelling and Analysis of a Semi-Submersible Floater Supporting the DTU 10MW Wind Turbine. Master's Thesis, Norwegian University of Science and Technology, Trondheim, Norway, 2016.
22. Zhu, Y. *Wave Mechanics in Ocean Engineering*; Tianjin University Press: Tianjin, China, 1991.
23. Liu, Y. *Research on Structural Strength Analysis Method of Single-Column Floating Wind Turbine*; Shanghai Jiao tong University: Shanghai, China, 2014.
24. SESAM User Manual, HydroD v4.10. In Wave Load & Stability Analysis of Fixed and Floating Structures. 2020. Available online: https://manualzz.com/doc/7321164/det-norske-veritas-hydrod-user-manual (accessed on 1 November 2024).

25. Sang, S.; Yu, M.; Shi, X.; Yi, S.; Yang, S.; Fei, S. Structural Strength Calibration of Semi-submersible Floating Wind Turbine Based on the Design Wave Method. *Acta Energiae Solaris Sin.* **2019**, *40*, 185–191.
26. Song, Z. *Structural Design and Dynamic Characterization of Large-Scale Floating Offshore Wind Turbine Platform*; Dalian University of Technology: Dalian, China, 2022.
27. *DNV GL-OS-C103*; Structural Design of Columnstabilised Units-LRFD Method. DNV GL: Høvik, Norway, 2020.
28. Wang, Y.; Xiu, S. Multi-objective optimization design of motor mounts applying response surface methodology. *Mech. Des. Manuf.* **2021**, *10*, 42–44.
29. Suresh, R.; Basavarajappa, S.; Samuel, G.L. Predictive modeling of cutting forces and tool wear in hard turning using response surface methodology. *Procedia Eng.* **2012**, *38*, 73–81. [CrossRef]
30. Ma, K.; Ren, F.; Wang, H.; Li, L.; Wu, D. Dynamic mechanical responses and freezing strengthening mechanism of frozen sandstone with single flaw: Insights from drop weight tests and numerical simulation. *Rock Mech. Rock Eng.* **2024**, *57*, 1263–1285. [CrossRef]
31. Liu, J.; Zhang, T.; Jin, P.; Zhu, B. Optimization of structural parameters of electric chain saw teeth based on Design-Expert. *For. Eng.* **2024**, *2*, 142–150.
32. Wang, J.; Ren, Y.; Shi, W.; Collu, M.; Venugopal, V.; Li, X. Multi-objective optimization design for a 15 MW semisubmersible floating offshore wind turbine using evolutionary algorithm. *Appl. Energy* **2025**, *377*, 124533. [CrossRef]
33. Quinlan, K.R.; Lin, D.K. Run order considerations for Plackett and Burman designs. *J. Stat. Plan. Inference* **2015**, *165*, 56–62. [CrossRef]
34. Yang, X.; Huang, S.; Shi, J.; Wang, B.; Wang, K.; Dong, S.; Li, H. Research on day-ahead electricity price prediction method based on dynamic data and multi-factor similarity day. *Electr. Power Big Data* **2024**, *27*, 35–44.
35. Lenth, R.V. Quick and easy analysis of unreplicated factorials. *Technometrics* **1989**, *31*, 469–473. [CrossRef]
36. Zhang, Z.; Li, Y.; Shi, L.; Wang, H. Improved response surface method and its application in structural reliability analysis. *Eng. Mech.* **2007**, *8*, 111–115+187.
37. Benalia, A.; Baatache, O.; Derbal, K.; Khalfaoui, A.; Amrouci, Z.; Pizzi, A.; Panico, A. The use of central composite design (CCD) to optimize and model the coagulation-flocculation process using a natural coagulant: Application in jar test and semi-industrial scale. *J. Water Process Eng.* **2024**, *57*, 104704. [CrossRef]
38. Verma, A.S.; Yan, J.; Hu, W.; Jiang, Z.; Shi, W.; Teuwen, J.J. A review of impact loads on composite wind turbine blades: Impact threats and classification. *Renew. Sustain. Energy Rev.* **2023**, *178*, 113261. [CrossRef]
39. Mustapha, A.; Mohamed, L.; Ali, K. An overview of gradient descent algorithm optimization in machine learning: Application in the ophthalmology field. In *Smart Applications and Data Analysis: Third International Conference, SADASC 2020, Marrakesh, Morocco, 25–26 June 2020*; Proceedings 3; Springer International Publishing: Cham, Switzerland, 2020; pp. 349–359.
40. Rezk, H.; Ferahtia, S.; Djeroui, A.; Chouder, A.; Houari, A.; Machmoum, M.; Abdelkareem, M.A. Optimal parameter estimation strategy of PEM fuel cell using gradient-based optimizer. *Energy* **2022**, *239*, 122096. [CrossRef]